Alan R. Gillespie
Anne B. Kahle
Jet Propulsion Laboratory
Pasadena, CA 91103

Construction and Interpretation of a Digital Thermal Inertia Image

Construction of the thermal inertia image requires specification of albedo, topographic slope and slope azimuth, diurnal temperature range, and local meteorological conditions.

Abstract: *An image representing the thermal inertia in the vicinity of Pisgah Crater and Lavic Lake in Southern California has been generated from visible, near IR, and thermal images taken from aircraft. Construction of the thermal inertia image required radiometric calibration and geometric rectification of the acquired images as well as registration to a topographic map. The Kahle thermal model used in the construction of the thermal inertia image requires specification of albedo, topographic slope and slope azimuth, diurnal temperature range and local meteorological conditions. Albedo information was derived from the visible image; digital topographic information was computed from digitized stereo aerial photographs; and thermal ranges were calculated by subtracting the predawn from the afternoon thermal image data. Our computed values of thermal inertia were in close agreement with published values for similar surface materials. Thermal inertia provides complementary information to conventional images of reflected solar radiation for use in lithologic mapping.*

Introduction

Thermal inertia is a measure of the resistance of matter to a change in its temperature. For a homogeneous material, this quantity can be expressed by $\sqrt{K\rho c}$, where K is the thermal conductivity, ρ is the density, and c is the specific heat. The use of thermal inertia in remote sensing is attractive because thermal inertia is a volume property, whereas many remotely sensed variables are properties of the surface alone. Consequently, knowledge of thermal inertia permits discrimination among different materials whose surfaces are similar. In geologic applications of remote sensing, the ability to sense below the surface is particularly desirable because exposed surfaces are often weathered or covered by thin layers of other materials.

Thermal inertia cannot be measured remotely and must therefore be inferred using models which have been developed to interpret remotely sensed visible and thermal radiation. Such a model has been developed by Watson (1971, 1973, 1975) for geologic applications, and applied by Pohn *et al.* (1974) to create a thermal inertia contour map from Nimbus III and Nimbus IV re-

Photogrammetric Engineering and Remote Sensing,
Vol. 43, No. 8, August 1977, pp. 983-1000.

flected solar radiation and thermal emission data. In spite of the low spatial resolution of Nimbus data (8 km), Pohn *et al.* were successful in recognizing lithologic differences. A different model has been developed by Kahle and is described fully elsewhere (Kahle, 1977). The Kahle model represents an improvement over previous models developed for geologic applications of thermal inertia, because it considers transfer between the ground and the atmosphere of latent and sensible heat in addition to the radiative transfer. We have used this model with remotely sensed thermal and reflective multispectral data of the Pisgah Crater-Lavic Lake region in the Mojave Desert of Southern California to develop techniques for displaying thermal inertia as a digital image.

A digital image is simply a sampled scalar field, with the field strength represented by an integer "date number," or "DN." This format provides information in a readily accessible data base for comparison and correlation with other remotely sensed data in similar format. The use of digital images and image processing in the interpretation of remotely sensed visible and near-visible data has been extensively reported by Rindfleisch *et al.* (1971), Rowan *et al.* (1974), Goetz *et al.* (1975), and Soha *et al.* (1975).

While digital images can be displayed as computer printouts of these numbers, a more effective display is achieved by using the DN at each sampled point to modulate a light source that exposes a photographic film. The exposed film, when developed, superfically resembles a normal photographic image. However, in a normal photographic image, scene detail is represented by continuous changes in the number density of opaque grains in the emulsion. In a photographic representation of a digital image, scene detail is represented by changes in average brightness of small areas in the emulsion called "picture elements," or "pixels."

For many purposes pictures have proven to be superior to computer printouts or other map forms representing image data because much more information can be displayed in a format that is convenient for human analysts, and because subtle spatial or textural relationships are more discernible. We believe that pictorial representation of thermal inertia data is desirable to take advantage of this enhanced display capability.

Construction of our thermal inertia image of Pisgah Crater-Lavic Lake, which was briefly reported by Kahle *et al.* (1976), required the following steps: (1) Acquisition of aerial photographs and ten channels of visible and one channel of digital thermal radiance data from the NASA NP3A aircraft using a Bendix Modular Multispectral Scanner (M^2S) in mid afternoon and also acquisition of the thermal radiance data alone at predawn; (2) Concurrent ground-based observation of albedo, surface and subsurface temperatures, soil moisture, and meteorological conditions; (3) Conversion of acquired M^2S data to digital computer compatible tapes at the Johnson Space Center in Houston; (4) Radiometric correction of M^2S image data to create albedo and temperature images; (5) Geometric rectification and registration of M^2S image data to conform to USGS topographic map geometry; (6) Creation of an afternoon-predawn temperature difference (ΔT) image; (7) Creation of a digital image of the altitude from stereo aerial photographs; (8) Prediction of ΔT using our model with the entire range of anticipated values of albedo, topography, and thermal inertia and the observed meteorological conditions; (9) Production, from the results of the model, of a look-up table which specifies thermal inertia as a function of albedo, topography, and ΔT; and (10) Creation of the thermal inertia image from the look-up table and the digital albedo, altitude, and ΔT images.

This paper presents a detailed description of the way in which this thermal inertia image was constructed and interpreted. Data processing is summarized in figure 1.

Data Acquisition

The Pisgah Crater-Lavic Lake region of southern California (figure 2) was selected as a test site for the thermal inertia model, and also for data acquisition leading to generation of our prototype thermal inertia image. The geology of this site is well known (e.g., Gardner, 1940; Gawarecki, 1964; Dibblee, 1966; Wise, 1966) and has been studied extensively using remote sensing techniques (Fischer *et al.*, 1965; Gawarecki, 1969; Sabins, 1969; Lyon, 1972; Vincent and Thomson, 1972). In addition, a desert environment, affording sparse vegetation, minimal cloud cover, and low humidity and soil moisture, was advantageous for the first test of our model.

Field measurements were made from 17-22 March 1975 and from 28-30 March 1975. Successful predawn and afternoon overflights were made on 29-30 March 1975 on two flight lines (figure 2) at altitudes of 1800 m and 4600 m by the NASA NP3A aircraft. Instrumentation on board consisted of

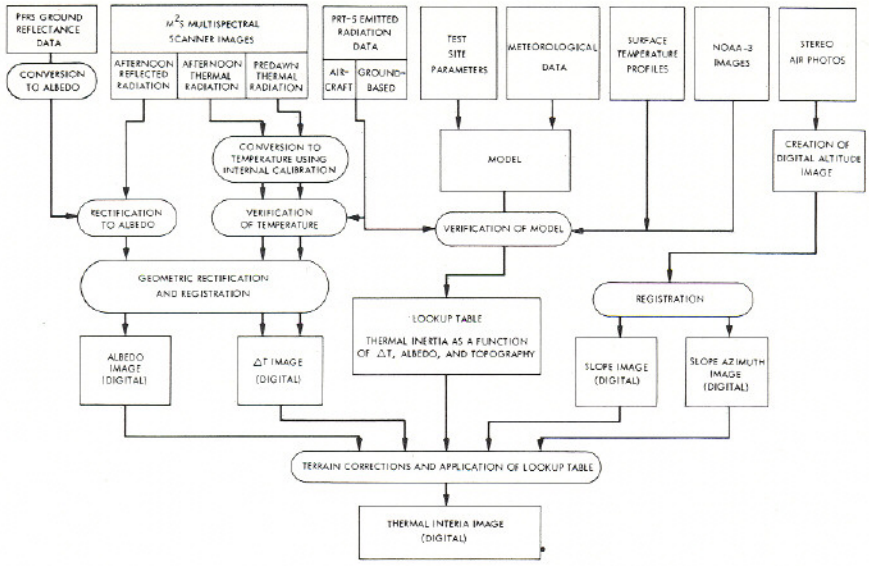

FIG. 1. Data processing diagram.

Zeiss cameras with film formats of 23 by 23 cm and focal lengths of 15 cm, a Barnes PRT-5 radiation thermometer, and the M²S (Table 1). The M²S acquired data in ten visible and near/IR spectral regions using silicon detectors and in one thermal region using a Hg-Cd-Te detector (Table 2). Electronic scanners such as the M²S generate images by rotating a mirror in front of the sensor in order to view from side to side as the aircraft or other vehicle moves forward (figure 3). The resultant image from a three minute data run consists of about 4 million pixels for each channel arranged in a rectilinear array of 800 samples and 5000 scan lines. The M²S scan subtends 100° and has an instantaneous field of view (IFOV) of 2.5 milliradians, which corresponds to an approximate scale of 3 m/pixel at the altitude of the low flight line. M²S data were transferred to digital computer compatible magnetic tapes at the Johnson Space Center in Houston.

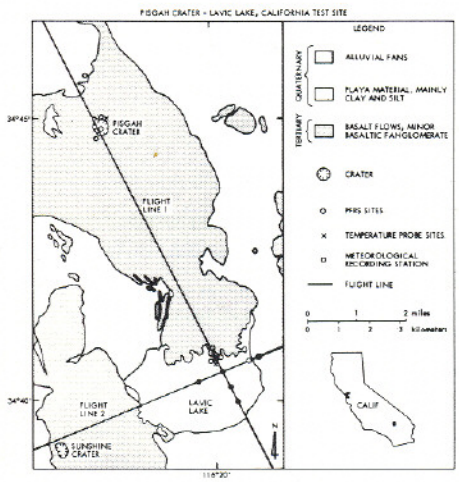

FIG. 2. Location map and simplified geology map of Pisgah Crater—Lavic Lake test site, (after Dibblee, 1966).

One channel of visible and one channel of thermal image data are acquired once and twice daily, respectively, by the VHRR scanner on board the NOAA-3 spacecraft, which flies over Pisgah Crater at approximately 9 a.m. and 9 p.m. The IFOV of the VHRR is about 1 km square at the subspacecraft point. We received digital VHRR data for 29-30 March 1975 from the NOAA/NESS Redwood City (California) office. These data were used to check the surface temperature of the test site at times of the day other than when the aircraft measurements were made, and appeared to verify the temperature predictions from the model, to within a couple of degrees.

The field observations provided meteorological, radiometric, and soil moisture and temperature data (Table 1). Some of the meteorological variables were recorded continuously while soil temperatures and other meteorological variables were recorded every two hours. Soil surface temperatures were determined radiometrically

TABLE 1. INSTRUMENTATION

	Instrument	Location	Variables Measured	Use
Image Data	Very High Resolution Radiometer (VHRR)	NOAA-3 Satellite	Reflected Solar Radiation; Thermal Radiance	Verification of Model
	Bendix Modular Multispectral Scanner (M^2S)	NP3A Aircraft	Reflected Solar Radiation; Thermal Radiance	Principal Data Source
	Zeiss Cameras f = 15.25cm	NP3A Aircraft	Reflected Solar Radiation	Generation of Digital Altitude Image; Geologic Interpretation
Local Radiation Data	JPL Portable Field Reflectance Spectrometer (PFRS)	Ground	Reflected Solar Radiation	Calibration of M^2S Reflected Radiation
	Barnes Precision Radiation Thermometer PRT-5	NP3A Aircraft	Thermal Radiance	Verification of M^2S Thermal Radiance
	Barnes Precision Radiation Thermometer PRT-5	Ground	Thermal Radiance	Verification of Model
	Eppley Pyrheliometer	Ground	Insolation	Verification of Model; Cloud Cover Estimation
Meterological Data	Meteorology Research Inc. Mechanical Weather Station	Ground	Wind Velocity, Air Temperature, Humidity	Meteorological Data For Model
	Thermographs	Ground	Air Temperature	Estimation of Spatial Variation of Meterological Parameters
	Hand-Held Venturi Gauges	Ground	Wind Speed	
	Sling Psychrometers	Ground	Air Temperature and Humidity	
	National Weather Service	Dagget, Calif.	Air Moisture Profile	Total Precipitable Water for Model
Soil Data	Temperature Probes: Thermometers and YSI Thermistors	Ground	Soil Temperatures	Verification of Model
	Soil Samples	Ground	Soil Moisture	Soil Moisture Content for Model

with a PRT-5, while subsurface temperatures were measured using thermistor probes at depths of 1 cm, 5 cm, 12 cm, 25 cm, and also at 40 cm or 50 cm as required. Subsurface temperature measurements at the eastern-most site on flight line one (figure 2) had to be discontinued after rodents gnawed through the thermistor leads. The MRI mechanical weather station recorded wind velocity, air temperature, and humidity continuously at one location on Lavic Lake (figure 2). Observations of temperature and wind speed were made at other sites every two hours. The Jet Propulsion Laboratory Portable Field Reflectance Spectrometer (PFRS) (Goetz *et al.*, 1975) was used to measure spectral reflectance from selected 200 cm^2 sites clustered near the locations indicated in figure 2. The PFRS data were used to determine surface albedo. We chose the PFRS sites to represent the entire range of surface materials encountered in the test site.

Soil samples for soil moisture determination were obtained on 17 March 1975 and

TABLE 2. SPECTRAL CHARACTERISTICS OF THE M^2S

Channel No.	Bandwidth (micrometers)
1	0.33 – 0.44
2	0.44 – 0.48
3	0.49 – 0.54
4	0.54 – 0.58
5	0.58 – 0.62
6	0.62 – 0.66
7	0.66 – 0.70
8	0.70 – 0.74
9	0.76 – 0.86
10	0.97 – 1.07
11	7.95 – 13.5

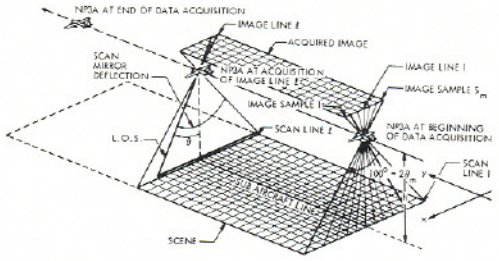

FIG. 3. Geometry of electronic scanner images.

again on 28 March 1975 from the same sites on Lavic Lake for which subsurface soil temperature profiles were made.

RADIOMETRIC CALIBRATION OF M²S IMAGE DATA

Radiometric calibration relates the measured scene radiance data *(DN)* to a desired variable. M²S image data consists of encoded scene radiance in eleven different spectral regions, and operation of our model required that these data be converted from radiance to albedo (for channels 1 to 10) or temperature (for channel 11). With large amounts of digital data, radiometric rectification and other image manipulations are most easily accomplished using digital computers. We used the VICAR image processing language (Jet Propulsion Laboratory, 1974) on an IBM 360-44 computer at the Image Processing Laboratory at JPL to perform all processing of the M²S image data.

For M²S channels 1 to 10, in the visible and near IR regions of the spectrum, the encoded, measured scene radiance is given by

$$DN_n = f\left(\int_{\lambda_1}^{\lambda_2} F_n(\lambda)R(\lambda)g(S[\lambda])d\lambda\right) \quad (1)$$

Where n refers to the M²S channel; λ is wavelength in micrometers; λ_1 and λ_2 are integration limits chosen to bracket the sensitivity of the M²S sensors (0.33 and 1.07 micrometers for channels 1 to 10); S is the solar irradiance; g is a function relating solar energy incident on the scene to illumination geometry, atmospheric absorption, and atmospheric scattering; R is the scene reflectance spectrum; F is the product of filter transmittance and scanner detector sensitivity; and f is a "light transfer function" which relates the measured to the actual scene radiance. Unfortunately, f was not described for M²S channels 1 to 10, nor was in-flight calibration provided, and we had to rely on ground reflectance data for calibration and had to assume that f was linear.

In general, radiometric calibration consists of compensating for f, and under some circumstances also for spectral response F, to determine the scene radiance from the measured *DN*. We used the PFRS to establish the geometric albedo at several sites contained in the imaged area which had obviously different $R(\lambda)$, and used these data to compensate for f and to produce a single "albedo" picture from the M²S visible and near IR radiance data.

We considered geometric albedo to be the ratio of the reflected to incident solar energy with vertical illumination and viewing angle and we assumed a Lambert surface:

$$A = \frac{\int_{\lambda_1}^{\lambda_2} R(\lambda)\, S(\lambda)\, d\lambda}{\int_{\lambda_1}^{\lambda_2} S(\lambda)\, d\lambda} \quad (2)$$

and we considered reflectivity to be the ratio of reflected to actual incident radiation, at a given wavelength

$$R(\lambda) = \frac{r(\lambda)}{g(S\ [\lambda])} \quad (3)$$

where $r(\lambda)$ was the vertically reflected radiance measured by the PFRS. However, because the actual incident radiation $g(S[\lambda])$ was a function of atmospheric conditions and illumination geometry, it varied with time, and in general would have to be determined to compute $R(\lambda)$. This was avoided by using the PFRS to measure the radiation reflected in the same direction from a calibration target composed of Fiberfrax ceramic wool, which was very nearly white in the visible and near IR spectrum. Because we assumed a Lambert surface, we can assume the bidirectional reflectivity determined with the PFRS is directly related to the albedo.

Thus we adopted the convention

$$A \approx A_f = \frac{\int_{\lambda_1}^{\lambda_2} R_f(\lambda)S(\lambda)d\lambda}{\int_{\lambda_1}^{\lambda_2} S(\lambda)d\lambda} \quad (4)$$

where the subscript f denotes normalization to the Fiberfrax standard; and

$$R_f(\lambda) = \frac{r(\lambda)}{r_f(\lambda)} \quad (5)$$

Figure 4 depicts $R_f(\lambda)$ determined by the

PFRS for basalts (Pisgah Crater) and playa clays (Lavic Lake), along with the associated M²S reflectivity which we calculated as described below.

We assumed that the albedo could be expressed as a linear combination of the *DNs* reported for each M²S channel, n,

$$A_f^{(i)} = \sum_{n=2}^{10} W_n^{(i)} DN_n^{(i)} \tag{6}$$

where we chose to exclude the first channel because it was excessively noisy and saturated. The albedo $A_f^{(i)}$ was known at each site (i) from the PFRS, and $DN_n^{(i)}$ were determined at each site by the M²S. We wished to use these data to compute the weighting functions $W_n^{(i)}$. These were computed separately for each PFRS station:

$$W_n^{(i)} = \frac{R_n^{(i)} F_n S_n}{DN_n^{(i)} \sum_{n=2}^{10} F_n S_n} \tag{7}$$

where $R_n^{(i)}$ is the average reflectivity for each channel, determined from the PFRS data, F_n is the filter function for each channel obtained from Johnson Space Center, and S_n is the average solar radiation in each channel, obtained from tabulated values. Finally a single weight $\overline{W}_n$ was chosen for each channel (Table 3) by averaging the individual weights for each channel from each site. Individual $W_n^{(i)}$ which were obviously deviant were discarded before averaging. These weighting functions thus calibrate the M²S data using PFRS data and also weight each channel according to its filter function and the solar spectrum.

After deriving these weighting functions, a digital albedo image was created using the computer to apply the algorithm

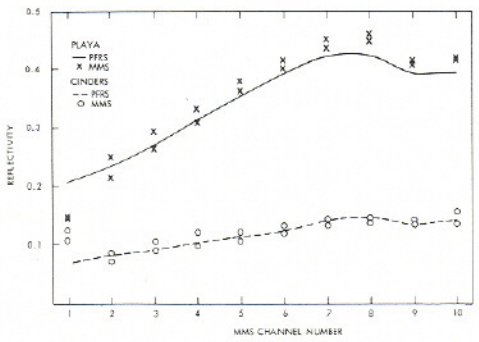

FIG. 4. Reflectivity of selected areas from PFRS and weighted M²S values.

$$A_f = \sum_{n=2}^{10} \overline{W}_n DN_n \tag{8}$$

at each pixel in the M²S nine-channel radiance image. Figure 5 shows the channel 5 radiance image, and figure 6 shows the corresponding albedo image. The noticeable horizontal striping was caused by noise in the scanner data. Topographic effects were ignored in constructing this image, although strictly

$$A'_f = A_f \cos^{-k} z' \tag{9}$$

where A'_f is the corrected albedo, z' is the incident angle of the solar radiation on a sloping surface, and k is the Minnaert coefficient, which is unity for a Lambert surface (Cf. equation 18). For the purposes of this study, we assumed $k = 1$, but for most real surfaces this is not true, and in future work some attempt may be made to estimate k, using remote sensing techniques described by Young and Collins (1971). In order to minimize computing costs, construction of the A'_f image was deferred until the actual construction of the thermal inertia image.

Unlike the visible and near IR channels (1 to 10), the M²S thermal channel was calibrated in flight by recording the *DN* reported every scan when the sensor monitored the radiance from two blackbodies set at different temperatures which bracketed the temperatures anticipated in the scene at the time of data acquisition. The actual temperatures of the blackbodies were independently monitored by thermistors and recorded automatically along with the radiance sensed by the scanner. In addition, the flight engineer recorded by hand in the flight log the intended blackbody temperatures. This was fortunate, because during afternoon flights the "hot" blackbody saturated its recording system, and consequently the blackbody

TABLE 3. WEIGHTING FUNCTION FOR M²S CHANNELS

Channel	Weighting Function
2	0.000155
3	0.000338
4	0.000304
5	0.000333
6	0.000288
7	0.000364
8	0.000269
9	0.000198
10	0.000125

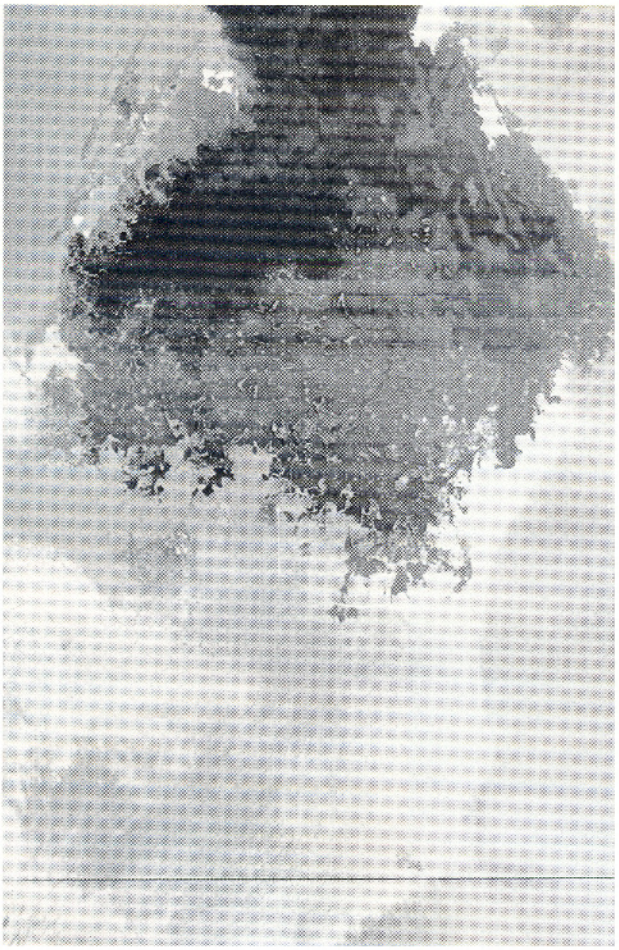

FIG. 5. M²S channel 5 radiance, detail of end of basalt flow (top) and Lavic Lake playa (bottom).

temperature recorded by hand had to be used for calibration. These hand-recorded temperatures agreed with the automatically recorded thermistor measurements to about one degree, when the recording system was operating. Blackbody temperatures were inferred from the encoded unsaturated thermistor voltages.

The surface temperature can be related to thermal radiance by the Stefan-Boltzmann law:

$$T = \left(\frac{r_t}{\epsilon\sigma}\right)^{1/4} \tag{10}$$

where ϵ is emissivity, which we assumed for simplicity to be 1.0 at all wavelengths; σ is the Stefan-Boltzmann constant; T is temperature; and r_t is the thermal radiance. Because DN_{11} (the DN value of channel 11) was reportedly linear with r_t, it was possible to convert DN_{11} to temperature:

$$T = (aDN_{11} + b)^{1/4} \tag{11}$$

where a and b are constants determined from the (DN_{11},T) pairs obtained during calibration.

Neither the blackbody temperatures nor the associated DN_{11} changed significantly during the 3-minute data runs, so the values of a and b were essentially constant and therefore determined only once per image. Figures 7a and 7b show derived temperature images for the pre-dawn and afternoon flights; lighter gray levels correspond to higher temperatures.

Temperature image accuracy was verified by comparison with both airborne and

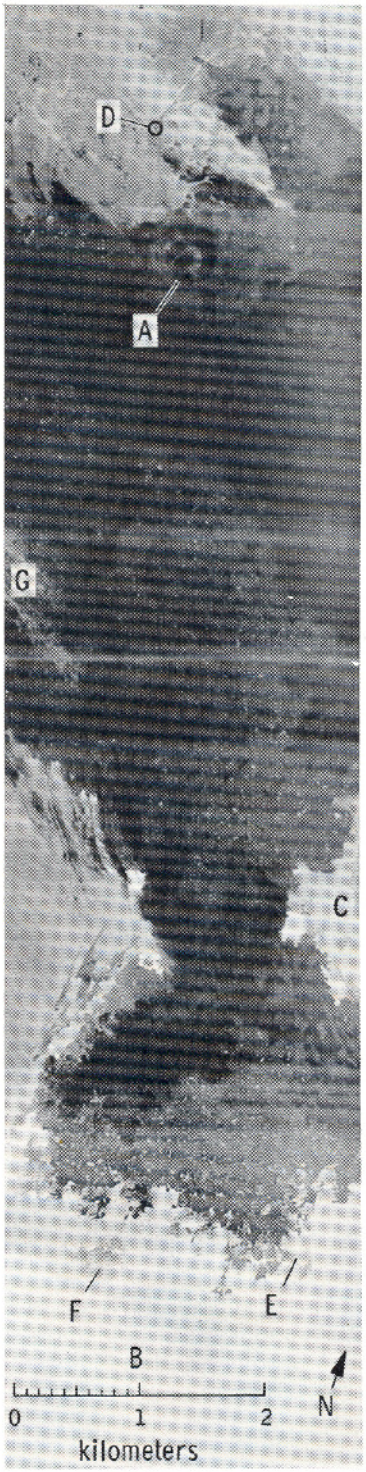

ground-based PRT-5 temperature data. No attempt was made to compensate for atmospheric effects. During verification of the temperature images, we discovered an east-west gradient in the south-north flight lines (figure 7b) which appeared in neither the predawn data nor data from another flight line in the east-west direction flown a few minutes later on the same afternoon. We believe this is an artifact which may be caused by heat radiated into the sensor at certain sun-aircraft orientations. The temperature gradient could be suppressed by normalization of the measured temperature at each sample, to the average temperature at that sample in all scans over a large, relatively homogeneous portion of the scene, assuming that the temperature along the subaircraft line was correct.

Adjustment of the thermal data to produce a temperature image was accomplished using the computer to apply equation 11 to the M²S radiance image.

We made no attempt to remove either random or systematic noise from the M²S image data. Random noise (e.g., bit errors) was minimal, but systematic noise correlated with scan lines was noticeable in M²S channels.

Geometric Rectification and Registration of M²S Images

Geometric rectification removes from images the systematic geometric distortions introduced by camera optics, viewing geometry, or platform motion. Rectification may also include projection of image data to a standard cartographic format. Geometric registration removes residual distortions which may remain on rectified images, so that the locations of features on an image coincide with their locations on a reference map or image.

Both geometric rectification and registration are best accomplished by resampling the image, and we did this using linear or bilinear interpolation, as described in Goetz *et al.* (1975).

Rectification of the M²S images consisted of removing foreshortening (panorama effect) caused by the changing viewing geometry with deflection of the scan mirror (Figure 3). Scene radiance was sampled at equal increments of time by the M²S, so that the distance between pixel centers, projected onto the imaged scene, decreased from the sides of the image (maximum scan mirror deflection) to the center of the image (minimum deflection). For a planar scene, and ignoring aircraft attitude errors, this effect can be described by:

$$\frac{s-1}{s_m-1}=\frac{\theta_m+\theta}{2\theta_m} \tag{12}$$

where s is the sample number in the acquired image, s_m is the maximum sample number in the acquired image, θ_m is the maximum scan mirror deflection (50°), and θ is the scan mirror deflection during the acquisition of sample s. θ can be related to the sample number s' in the rectified picture, in which the sample scale is constant, by

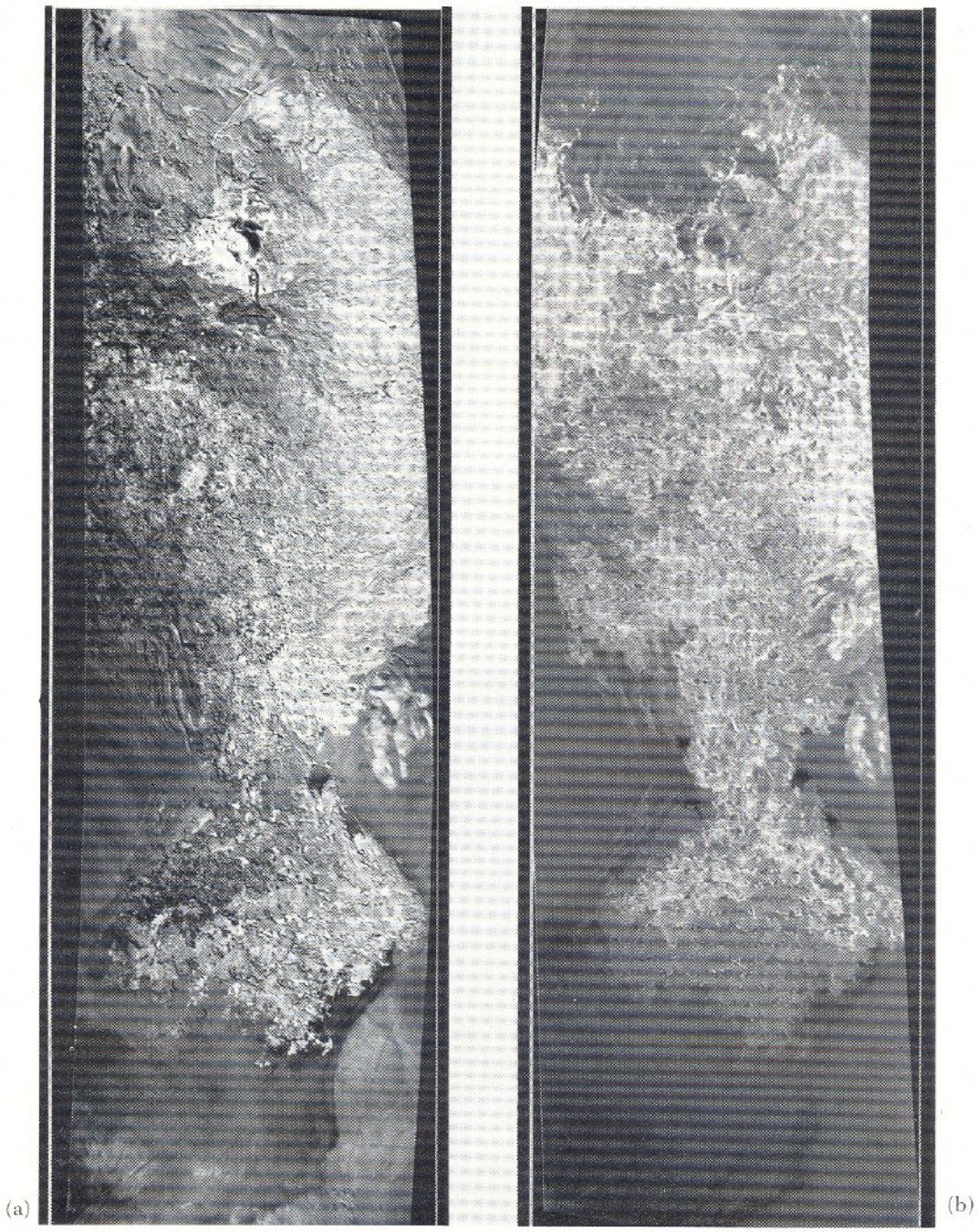

(a) (b)

FIG. 7. Temperature images (a) pre-dawn and (b) afternoon. Curved boundaries are a result of geometric corrections.

$$\theta = \tan^{-1}\left[\frac{2s' - (s'_m + 1)}{2h}\right] \quad (13)$$

where h is the height in pixels to the aircraft, and s'_m is the total number of samples in the rectified picture. Because the signal is sampled at equal time increments, or equal increments of θ,

$$h = \frac{s_m - 1}{2\theta_m} \quad (14)$$

and because the scale is constant in the rectified image,

$$s' = h \tan \theta_m \quad (15)$$

Substituting from equations (13), (14), and (15) into equation (12),

$$s = 1 + \frac{(s_m - 1)}{2\theta_m} \cdot \left[\theta_m + \tan^{-1}\left(\frac{2\theta_m}{s_m - 1}(s' - 1) - \tan \theta_m\right)\right] \quad (16)$$

which identifies the position in the acquired image from which the *DN* at sample s' in the rectified image must be extracted. These computed positions fall between samples, so the correct *DN* in the rectified image must be found by interpolation. The acquired and rectified temperature images for part of one flight line are shown in figures 8a and 8b.

Large residual geometric errors were found after rectification, and we attributed these to unavoidable attitude and range changes in the aircraft during data acquisition caused in part by air turbulence, parallax, and changes in range as the aircraft flew over regions having topographic relief. These residual errors were identified and removed during registration.

There were three sets of unregistered images: the afternoon albedo and temperature images, which had identical geometry because they were acquired by the same instrument at the same time, the predawn temperature image, and an altitude image constructed from the stereo air photos (discussed below). We first registered each image to the USGS 1:24,000 scale topographic map, locating control points or features recognizable in both the map and the images with the aid of a coordinate digitizer. For pixels not corresponding to control points, the geometric distortion was estimated by bilinear interpolation from the measured distortions at the nearest control points. Once the location on the unregistered image corresponding to each pixel in the reference map (or in the registered image being constructed) was found, the registered image

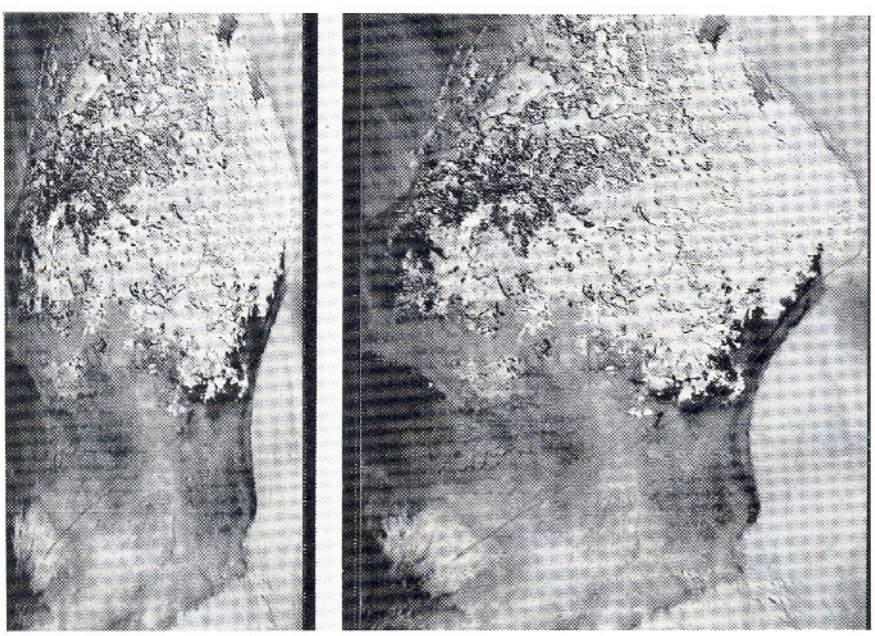

(a) (b)

FIG. 8. Temperature images, detail of end of basalt flow (a) before, and (b) after panorama rectification.

was created using bilinear interpolation to compute the correct *DN*.

After registering all images to the topographic map, the predawn temperature image and the altitude image were registered to the afternoon temperature image, using automated cross-correlation techniques to determine remaining misregistration at selected control points. This was required because the image resolution was much higher than that of the topographic map. We estimate the remaining registration error between the day and night images to be less than two pixels. The registration to the topographic map is necessarily less accurate because of lack of detail on the map.

More complete discussions of geometric corrections are available in Goetz *et al.* (1975), while discussion of the VICAR cross-correlation registration program "REGISTER" is found in Schwartz (1972).

Construction of ΔT Image

Construction of the ΔT image was accomplished by subtracting, pixel by pixel, the registered predawn temperature image from the afternoon temperature image.

Figure 7a and 7b show the predawn and afternoon temperature images, and figure 9 shows the ΔT image created from them.

Construction of Altitude Image

A digital image describing scene altitude was constructed in the form of a square grid digital terrain model (DTM) with a sample interval equal to that of the M²S image. The terrain data were acquired photogrammetrically using wide-angle metric photographs taken simultaneously with the scanner data, at a scale of 1:12,000. The elevations were sampled along parallel, equidistant profiles and recorded in digital form using standard stereo-photogrammetric procedures. Random errors of the photogrammetric measurements of the altitude can be expected to be about ±30 cm (1 standard deviation). The DTM was constructed from the discrete, digital profiles using a simple and fast pointwise interpolation algorithm particularly well suited to profile data: at each pixel, a height was interpolated using the 16 closest available data points, which defined a polynominal of third order. The algorithm was thus similar to the "moving-average" method used in work with random functions (Yaglom, 1962). The errors in the interpolated elevations were less than 1 to 2 meters. We constructed the altitude image to include only Pisgah Crater and its immediate vicin-

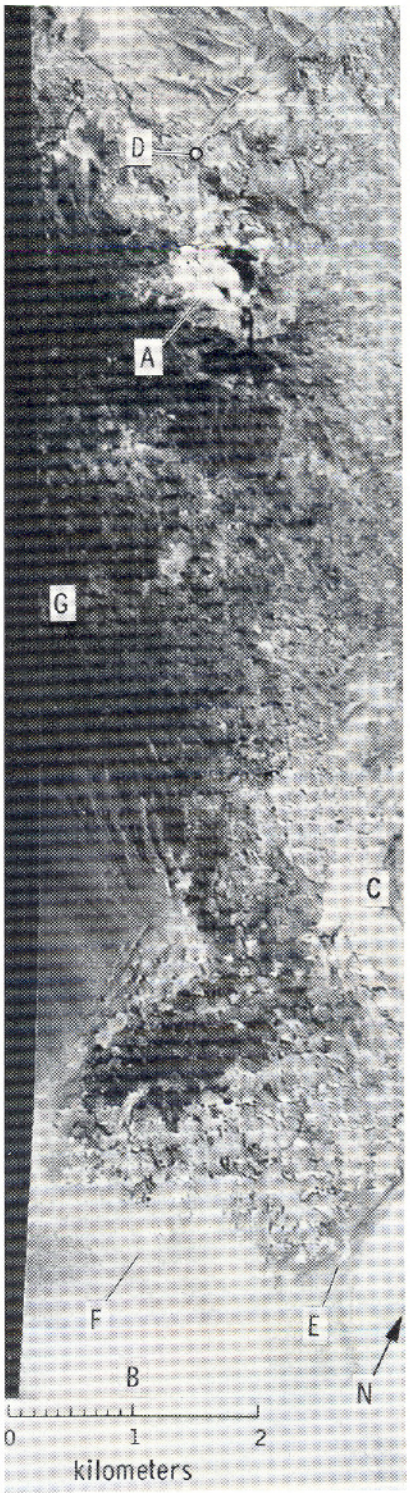

FIG. 9. Image of difference between afternoon and pre-dawn temperature (ΔT).

ity; elsewhere in the test site terrain relief was negligible at the M²S image scale and at the accuracy required by the thermal inertia model. Figure 10a shows the altitude contours from this digital altitude image, superposed on the albedo image of Pisgah Crater, and the brightness in figure 10b shows computed insolation at Pisgah Crater based on the altitude image, assuming a Lambert surface of constant albedo.

From the digital altitude image we derived two images describing slope and slope azimuth. These values were computed at each pixel by determining the gradient from the four nearest pixels.

We thus created four registered images (albedo, ΔT, slope, and slope azimuth), each containing approximately 6 million pixels. The thermal inertia was determined from these data sets by application of the model as described in the next two sections.

Model Prediction of ΔT and Generation of Thermal Inertia Table

We used our model (Kahle, 1977) to predict ΔT as a function of thermal inertia, albedo, slope, and slope azimuth, for a complete range of these variables (Table 4). The soil moisture measurements indicated 2 to 4 percent moisture by weight in the cinder cone and alluvial fans from the surface to a depth of 50 cm while the moisture profile on the playa averaged as follows: depth 1 cm, 6 percent; 5 cm, 8 percent; 12 cm, 10 percent; and 25 cm, 12 percent. Because of the low moisture everywhere except on the playa, and because we were primarily interested in demonstrating the feasibility of constructing a thermal inertia image, we chose to ignore soil moisture effects. These effects, including primarily change in thermal properties of the surface and evaporative cooling, will be included in later versions of our modeling. The meteorological variables were measured over the entire site, but only the values of the air temperature and wind speed recorded at Lavic Lake were used in the model. Measurement of air temperature and wind speed at other locations indicated that they did not vary sufficiently across the test site to require running the model for more than one set of meteorological data.

Nevertheless, running the model, which numerically integrates the one-dimensional heat flow equation over a 48 hour period in one-to two-minute steps for each combination of the variables in Table 4 ($8^4 = 4096$ combinations), was exceedingly time consuming, taking approximately four hours on an IBM 370-158. We also tested the model on an IBM 360-44 and an IBM 1130 where we estimated it would require 24 hours and 600 hours of computer time, respectively.

Because this was the first test of our model over the complete range, we did not know, *a priori*, the number of values of each of the variables in Table 4 which would be required to define ΔT. After the model was run, generating the four-dimensional table predicting ΔT, we determined that fewer

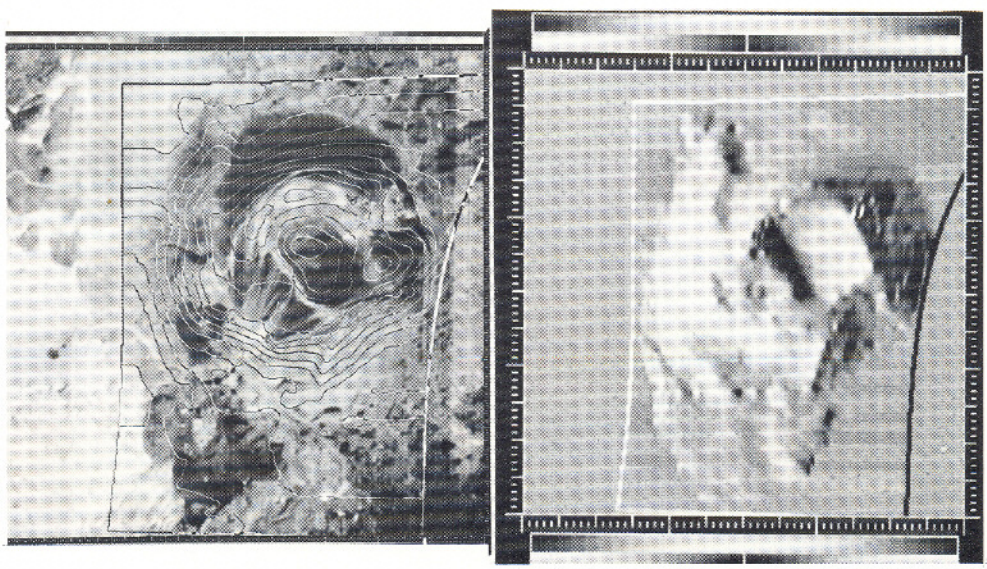

Fig. 10. (a) Altitude contours superposed on albedo image at Pisgah Crater. (b) Computed insolation at Pisgah Crater. North at left.

TABLE 4. RANGE OF PRINCIPAL VARIABLES IN MODEL

Variable	Range	Step-Size
Thermal Inertia	0.004–0.088 cal $cm^{-2°}K^{-1}sec^{-1/2}$	0.012
Albedo	0.04 –0.60	0.08
Slope	0°–28°	4°
Slope Azimuth	9°–315°	45°

values of the variables could have been used in all cases, except for slope azimuth. The dependence of ΔT on thermal inertia, albedo, and slope was slowly varying and almost linear, so that only three values of each of these variables need have been run in the model. The intermediate values could then have been found by interpolation. However, construction of a satisfactory thermal inertia image required the azimuth to be sampled more often than every 45°, and we accomplished this by linear interpolation between values computed by the model. The dependence of ΔT on slope azimuth was approximately a one-cycle sine curve, allowing us to interpolate to every 5°. Thus, if interpolation is used where feasible, it appears that only 216 integrations ($3 \times 3 \times 3 \times 8$) rather than the 4096 integrations originally used will be required in future studies. This will reduce the computer time by an order of magnitude.

We also found, after the model was run, that slopes up to 36° were present at Pisgah Crater, so the table was extrapolated to include these steeper slopes.

Once constructed, the four-dimensional table of ΔT as a function of thermal inertia, albedo, slope, and slope azimuth was reformatted using linear interpolation to create a table of thermal inertia as a function of ΔT (in 1° steps from 0° to 64°), albedo, slope, and slope azimuth. This table was then used with our four digital images depicting those variables to create a thermal inertia image as described in the next section.

CONSTRUCTION OF THE THERMAL INERTIA IMAGE

The thermal inertia image was created by using the *DN* values from the albedo, topographic slope and slope azimuth, and ΔT images to compute addresses in the lookup table. However, we first had to compensate the albedo image for effects of viewing and illumination geometry. As long as the scene consists of a Lambert surface (Minnaert $k = 1$), the apparent, measured albedo in line scanner images is essentially independent of viewing geometry, because the IFOV varies with the reciprocal of cos e (where e is the "emergent" angle, or the angle from the sensor to the local surface normal) while the radiant flux per unit area varies with cos e itself so that the two cos e terms cancel. However, as shown in equation 9, the albedo is a function of cos z', where z' is the incident angle of solar radiation on a sloping surface.

$$\cos z' = \cos s \cos z + \sin s \sin z \cos (\phi - \phi_o) \tag{17}$$

where s is the slope, z is the solar zenith angle, ϕ is the slope azimuth, and ϕ_o is the solar azimuth. Thus, when creating the thermal inertia image from the table, the topography at the point was determined first. Next, equation 9 was applied to correct the albedo for the incident angle of solar radiation. Then the thermal inertia was found in the lookup table.

If the real surface cannot be approximated by a Lambert surface, then equation 9 must be modified to compensate for viewing geometry also:

$$A'_f = A_f \cos^{-k} z' \cos^{1-k} e \tag{18}$$

where A_f is the measured albedo and A'_f is the corrected albedo. The emergent angle e may be found if the flight azimuth, scan mirror deflection θ (defined in equation 13), and the local surface slope and slope azimuth are known:

$$e = \theta + s \cos [\phi - (\phi_f - 90°)] \tag{19}$$

where ϕ_f is the azimuth of the flight line. The constant 90° converts ϕ_f to the azimuth of the scan line. For this experiment, we used the approximation of a Lambert surface, so only the correction from equation 9 was required.

The thermal inertia image is shown in figure 11, where different gray levels represent different values of thermal inertia. With the exception of Pisgah Crater itself, the topographic gradients were minimal. Therefore, for economy, the topography was not

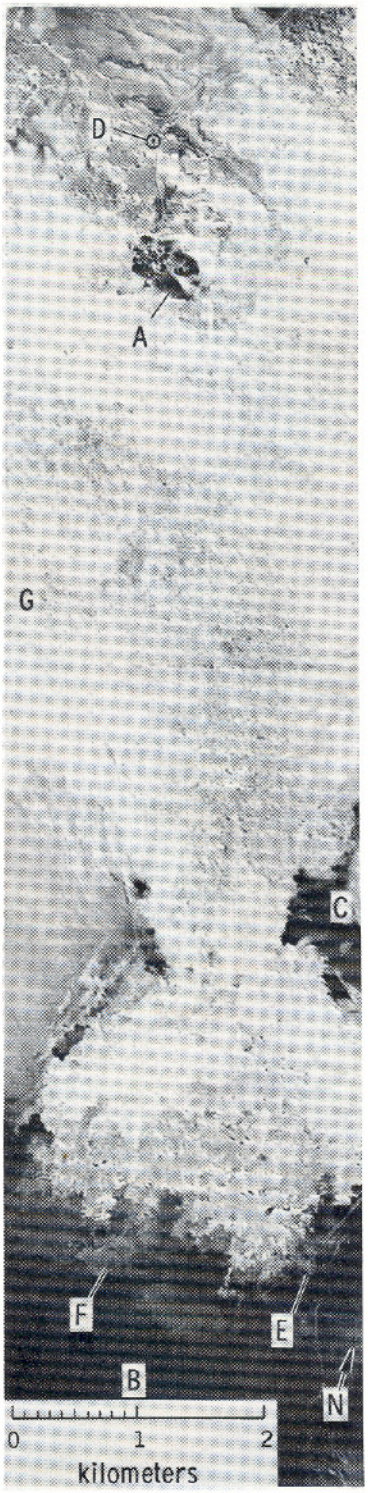

FIG. 11. Thermal inertia image.

included in the construction of the thermal inertia image in figure 11. Instead, the thermal inertia image was constructed a second time, in the immediate vicinity of Pisgah Crater only, with the inclusion of digital topography. A first attempt was made using the commercially available 1:250,000 NCIC digital altitude data which is shown in figure 12 as an elevation contour map overlaid on the digital altitude image. This image did not provide sufficient resolution at the scale of the M²S imagery so we used the digital topography derived from the aerial photography. The two thermal inertia images of this area, without and with topographic corrections, are shown in figures 13a and 13b. The difference in thermal inertia is shown in figure 13c. These clearly demonstrate the necessity for such corrections in regions of moderate to higher relief. In the uncorrected version (figure 13a), the crater appears anomalously bright on the east-facing side and dark on the west-facing side. This effect occurs because, as shown in the albedo image (figure 6), the east side already was shaded when the afternoon images were acquired, while the west side was fully illuminated. Thus the east side was cooler than horizontal surfaces of the same substance (basalt cinders), while the west side was warmer, and these anomalous temperatures produced the anomalous thermal inertias. In the topographically compensated version (figure 13b) these effects are reduced, but still evident, especially on smaller features.

The digitized altitude image derived from the stereo aerial photographs was constructed to have the same spatial resolution as the M²S images, approximately 3m by 3m. This altitude image was derived by interpolation, as described in an earlier section, from equidistant profiles across contour lines, with a profile spacing of about 15 m. Thus the altitude image was "smooth" relative to the M²S imagery. Topographic effects on the heating, caused by topography at a scale comparable to the M²S image resolution, were therefore not compensated. These effects are responsible for most of the remaining structural detail seen in figure 13b. Similarly, the basalt flow, which dominates the scene and for which topographic corrections were not applied because of the gentle average slope, shows detailed dark and light patterns due to the small-scale, very rough, blocky nature of the surface (figure 11). Although the failure to compensate for the small scale topographic effects is useful in giving us textural information, it does reduce the local validity of the calculated thermal

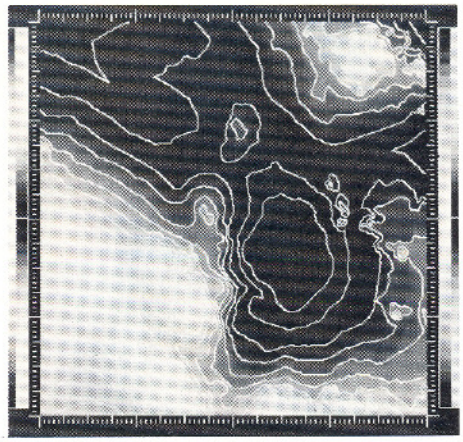

FIG. 12. NCIC digital altitude image, with north at top. Lavic Lake is at right center, with Pisgah Crater represented by two isolated concentric contours northwest of Lavic Lake.

inertia values.

Figure 14 is a simulated stereogram constructed from the 1:12,000 altitude image and the compensated thermal inertia image. This stereogram was produced by distorting the reference image (figure 14a), pixel by pixel an amount proportional to the distance of the ground from the aircraft, as determined from the altitude image. The resulting distorted image is shown in figure 14b. The simulated stereogram differs from a true stereogram in that neither the reference image nor the distorted image is in a simple perspective projection, as an aerial photograph would be. The reference image was registered to a Universal Transverse Mercator map, while the new image was distorted in one direction only, a feature also common to real stereograms from line scanners. The simulated stereogram demonstrates the lack of correlation between remaining thermal inertia variations and topography.

INTERPRETATION OF THE THERMAL INERTIA IMAGE

The dominant feature in both the albedo (figure 6) and thermal inertia picture (figure 11) is the Pisgah basalt flow. This flow, which extends from Pisgah Crater (feature A in the illustrations) south to Lavic Lake (feature B) has a low albedo (0.06 - 0.13) but a relatively high calculated thermal inertia (0.04 - 0.08 cal $cm^{-2}°K^{-1}sec^{-1/2}$). It is thus dark in the albedo picture and light in the thermal inertia picture. The areas on the basalt flow having higher thermal inertia (the lighter gray on the image) are generally partially covered with mixed layers of sand and broken basalt. Lavic Lake, a clay playa, has a high albedo (0.35 - 0.50) but a low calculated thermal inertia (0.01 - 0.03 cal $cm^{-2}°K^{-1}sec^{-1/2}$). It is thus light in the albedo picture and dark in the thermal inertia picture. Histograms depicting the discrete probability density function (PDF) (the frequency of occurrence) of the albedo and thermal inertia values in these images are reproduced in figures 15a and 15b, and clearly show the bimodal character of the thermal inertia value distribution. A typical value of the thermal inertia of basalt, given by Janza (1975), is 0.053 cal $cm^{-2}°K^{-1}sec^{-1/2}$, and for dry clays the thermal inertia is about 0.010 to 0.017 cal $cm^{-2}°K^{-1}sec^{-1/2}$ (Kenneth Watson, written communication, 1974). These values are in close agreement with the values computed using our model. For wet clays, however, the thermal inertia is somewhat higher, and our calculated playa

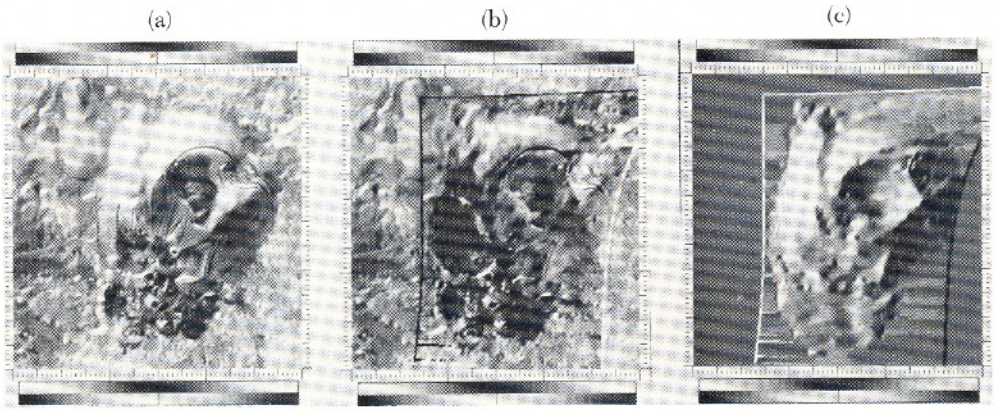

FIG. 13. Thermal inertia at Pisgah Crater (a) without, and (b) with topographic correction, (c) difference in thermal inertia with and without topographic correction. North at left.

FIG. 14. Simulated stereogram at Pisgah Crater. North at left, vertical relief exaggerated.

values range from 0.01 to 0.03 cal $cm^{-2}°K^{-1}sec^{-1/2}$, covering the range we might expect. However, in our model as used here, the variation of the thermal properties of the surface with depth due to increased moisture was ignored, as was the evaporative cooling. Thus the absolute value of the thermal inertia on the playa is open to question.

The use of ΔT rather than the actual values of the surface temperature in our method for determination of thermal inertia minimized errors introduced by ignoring surface emissivity and atmospheric transmissivity.

A strong correlation exists in these images between areas with low albedo (dark) and high thermal inertia (light). This is illustrated by the two-dimensional PDF of a portion of the scene, shown in figure 16. Positively correlated data will fall along a line with a positive slope; negatively correlated data will fall along a line with a negative slope; and uncorrelated data will be scattered over the whole diagram. Figure 16 shows both the dominant negative correlation which exists between thermal inertia and albedo in the Pisgah Crater-Lavic Lake area and also significant deviations from this rule. All the basalt lies in the upper left part of the diagram, while the playa lies in the lower right. No cinders were present in the part of the scene represented here, but they would fall in the lower left part of the diagram. The negative correlation is not an artifact of our model, but a coincidence at this particular site because of the type of rock and soil present. Had the site contained high-albedo granite instead of dark basalt, for instance, the thermal inertia picture would be essentially unchanged (the thermal inertia for granite is about 0.06 cal $cm^{-2}°K^{-1}sec^{-1/2}$) but the albedo picture would be much different.

Deviation from the negative correlation between albedo and thermal inertia is best illustrated at location D, where there was an area of basalt cinders used as road fill. These cinders have both a low albedo and a low thermal inertia. Other cinders, especially in the flat area immediately northwest of the cinder cone, likewise have both low albedo and low thermal inertia, and can be readily distinguished from the basalt flows, which have low albedo but high thermal inertia. In the topographically uncompensated image (figure 13a) the topographic effect on the solar heating tends to obscure the thermal inertia effects at the cinder cone itself. In the compensated image (figure 13b) this effect has been reduced, and the low thermal inertia region corresponds to disturbed cinders in a quarry. Similarly, the road visible on the east flank of the cinder cone and which is

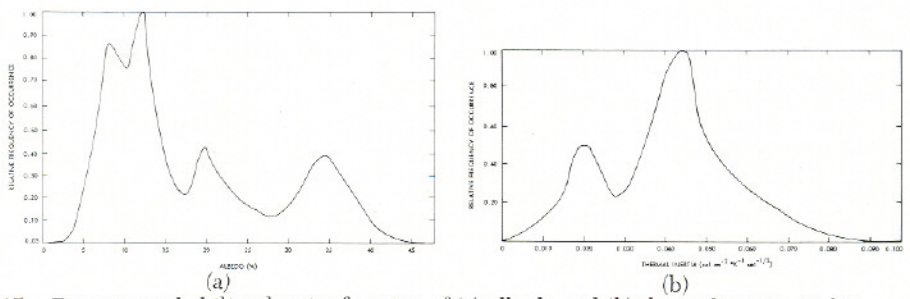

(a) (b)

FIG. 15. Discrete probability density function of (a) albedo and (b) thermal inertia. Relative units.

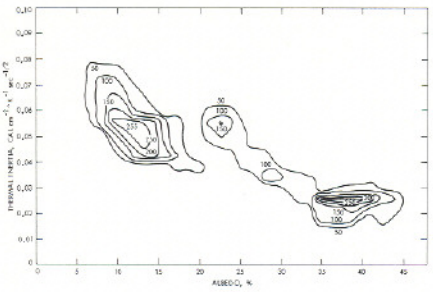

FIG. 16. Two-dimensional probability density function of albedo and thermal inertia. Relative units.

constructed of crushed cinders has a lower thermal inertia than the undisturbed cone.

Examination of the two images at several locations where one material is overlain by a thin layer of a different material (locations E, F, G) shows that the resultant value of the thermal inertia is either intermediate between the two or, for a very thin surface layer, resembles the thermal inertia of the underlying material. Locations E and F show some examples of intermediate values of thermal inertia at the boundary between the lava flow and the playa, where a few centimeter thick outwash of basalt overlies the playa. At location G, where a very thin layer of sand has blown across the basalt, the thermal inertia is representative of the underlying basalt.

Thus, the usefulness of thermal inertia information is in distinguishing between materials of similar reflective properties but different thermal properties, and in assisting in the identification of surface materials which are covered with a thin layer of foreign matter, especially wind blown sand or dust or weathering products such as desert varnish. It is clear that, by itself, thermal inertia is not sufficient to allow identification of surface materials, but when interpreted in conjunction with conventional imagery it is of considerable value in resolving ambiguities.

In summary, we have produced a thermal inertia image from remotely sensed thermal and reflected radiation data augmented with ground measurements of meteorological variables, and demonstrated some of the possible geologic applications of thermal inertia images. A knowledge of thermal inertia of the surface material is not sufficient for geologic mapping. However, it can be used in combination with remotely sensed thermal emissivity and visible and near-infrared spectral reflectance data, in addition to conventional aerial photography, for discrimination of broad compositional categories of rocks in reconnaissance geologic mapping.

ACKNOWLEDGMENTS

The authors would like to thank the numerous people who assisted in this project. M. Molloy, T. Fischetti, L. Jaffe, and B. Nolan of NASA Headquarters made the aircraft flights possible. J. Quade, a consultant to JPL, led the field work. Also assisting in the field work were S. Levine, S. Marsh, and G. Ballew of the Stanford Remote Sensing Laboratory. G. Hrabal of the Johnson Space Center (JSC) was the aircraft mission manager, and R. K. Stewart and R. Ligons provided rapid data handling at JSC. L. Breaker of NOAA/NESS supplied the NOAA-III VHRR digital data. JPL personnel involved in the field work and/or the data analysis included A. Goetz, J. Schieldge, J. Addington, M. Morrill, J. Soha, H. Paley, E. Abbott, F. Leberl, M. Abrams, and B. Siegal. The U.S. Marine Corps and the Lavic Stone Corporation allowed us access to their land.

This paper presents the results of one phase of research carried out at the Jet Propulsion Laboratory, California Institute of Technology under Contract Number NAS 7-100, sponsored by the National Aeronautics and Space Administration.

REFERENCES

Dibblee, T. W., *Miscellaneous Geological Investigations Map I-472*, U.S. Geological Survey, Washington, D. C., 1966.

Fischer, W. A., J. D. Friedman, and T. M. Sousa, Preliminary results of aerial infrared surveys at Pisgah Crater, California, U.S. Geological Survey, *Tech. Letter NASA-5*, 1965.

Gardner, D. L., Geology of the Newberry and Ord Mountains, San Bernardino County, California, *California J. Mines and Geology*, *36*, 257-292, 1940.

Gawarecki, S. J., Geologic reconnaissance report of the Pisgah Crater, California area, U.S. Geological Survey, *Tech. Lett. NASA-2*, 1964.

Gawarecki, S. J., Infrared survey of the Pisgah Crater area, San Bernardino County, California, A geologic interpretation, U.S. Geological Survey, *Tech. Letter NASA-99*, 1969.

Goetz, A. F. H., F. C. Billingsley, A. R. Gillespie, M. J. Abrams, R. L. Squires, E. M. Shoemaker, I. Lucchitti, and D. P. Elston, Application of ERTS Image Processing to Regional Geologic Problems and Geologic Mapping in Northern Arizona, Jet Propulsion Laboratory, *Tech. Rep. 32-1597*, Pasadena, Calif., 1975.

Janza, F. J., Chapter 4, Interaction Mechanisms, in *Manual of Remote Sensing*, R. G. Reeves, ed., p. 83, Amer. Soc. Photogrammetry, Falls Church, 1975.

Jet Propulsion Laboratory, Image Processing Laboratory User's Documentation of Applications Programs, Jet Propulsion Laboratory Internal Document 900-670, Oct. 11, 1974.

Kahle, A. B., A simple thermal model of the Earth's surface for geologic mapping by remote sensing, *J. Geophys. Res.*, in press, 1977.

Kahle, A. B., A. R. Gillespie, and A. F. H. Goetz, Thermal inertia imaging: A new geologic mapping tool, *Geophys. Res. Let.*, 3, 26-28, 1976.

Lyon, R. J. P., Infrared spectral emittance in geological mapping: Airborne spectrometer data from Pisgah Crater, California, *Science*, 175, 983-986, 1972.

Pohn, H. A., T. W. Offield, and K. Watson, Thermal inertia mapping from satellite-discrimination of geologic units in Oman, *Jour. Research U. S. Geol. Survey*, 2, 147-158, 1974.

Rindfleisch, T. C., J. A. Dunne, H. J. Frieden, W. D. Stromberg, and R. M. Ruiz, Digital processing of the Mariner 6 and 7 pictures, *J. Geophys. Res.*, 76, 394-417, 1971.

Rowan, L. C., P. H. Wetlaufer, A. F. H. Goetz, F. C. Billingsley, and J. H. Stewart, Discrimination of rock types and altered areas in Nevada by the use of ERTS images, U. S. Geol. Survey, Prof. Paper 883, 1974.

Sabins, F., Thermal infrared imagery and its application to structural mapping in Southern California, *Geol. Soc. Amer. Bull.*, 80, 397-404, 1969.

Schwartz, A. A., *Register–A User's Guide*, Jet Propulsion Laboratory IOM 824-IPL/72-302, 1972.

Soha, J. M., D. J. Lynn, J. J. Lorre, J. A. Mosher, N. N. Thayer, D. A. Elliott, W. D. Benton, and R. E. Dewar, IPL Processing of the Mariner 10 Images of Mercury, *J. Geophys. Res.*, 80, 2394-2414, 1975.

Vincent, R. K. and F. J. Thomson, Rock-type discrimination from ratioed infrared scanner images of Pisgah Crater, California, *Science*, 175, 986-988, 1972.

Watson, K., A Computer Program of Thermal Modeling for Interpretation of Infrared Images, *Rep. PB 203578*, 33 pp., U. S. Geol. Survey, Washington, D. C., 1971.

Watson, K., Periodic heating of a layer over a semi-infinite solid, *J. Geophys. Res.*, 78, 5904-5910, 1973.

Watson, K., Geologic applications of thermal infrared images, *Proc. IEEE*, 63, 128-137, 1975.

Wise, W. S., Geologic map of the Pisgah and Sunshine Cone lava fields, U. S. Geological Survey, *Tech. Letter NASA-11*, 1966.

Yaglom, A. M., *An Introduction to the Theory of Stationary Random Functions*, Rev. English edition Trans. & Ed. by Richard A. Silverman, Prentice-Hall, Englewood Cliffs, N. J., 1962.

Young, A. T., and S. A. Collins, Photometric properties of the Mariner cameras and of selected regions on Mars, *J. Geophys. Res.*, 76, 432-437, 1971.